arXiv:1403.5403v1 [cs.CV] 21 Mar 2014

A Non-Local Structure Tensor Based Approach for Multicomponent Image Recovery Problems

Giovanni Chierchia* Nelly Pustelnik† Béatrice Pesquet-Popescu*
Jean-Christophe Pesquet‡

March 24, 2014

Abstract

Non-Local Total Variation (NLTV) has emerged as a useful tool in variational methods for image recovery problems. In this paper, we extend the NLTV-based regularization to multicomponent images by taking advantage of the Structure Tensor (ST) resulting from the gradient of a multicomponent image. The proposed approach allows us to penalize the non-local variations, jointly for the different components, through various $\ell_{1,p}$ matrix norms with $p \geq 1$. To facilitate the choice of the hyper-parameters, we adopt a constrained convex optimization approach in which we minimize the data fidelity term subject to a constraint involving the ST-NLTV regularization. The resulting convex optimization problem is solved with a novel epigraphical projection method. This formulation can be efficiently implemented thanks to the flexibility offered by recent primal-dual proximal algorithms. Experiments are carried out for multispectral and hyperspectral images. The results demonstrate the interest of introducing a non-local structure tensor regularization and show that the proposed approach leads to significant improvements in terms of convergence speed over current state-of-the-art methods.

1 Introduction

Multicomponent images consist of several spatial maps acquired simultaneously from a scene. Well-known examples are color images, which are composed of red, green, and blue

*Institut Mines-Télécom, Télécom ParisTech, CNRS LTCI, 75014 Paris, France
†ENS Lyon, Laboratoire de Physique, UMR CNRS 5672, F69007 Lyon, France
‡Université Paris-Est, LIGM, UMR CNRS 8049, 77454 Marne-la-Vallée, France

components, in accordance to the ability of human psycho-visual system to perceive the visible light through three types of cone cells. By contrast to color photography, imaging spectroscopy extends beyond the visible light and divides the electromagnetic spectrum into many components that represent the light intensity across a number of bands or wavelengths. Spectral imagery is used in a wide range of applications such as remote sensing [1], astronomical imaging [2], and fluorescence microscopy [3].

Multicomponent imagery, including color photography and imaging spectroscopy, is often degraded by blur and noise arising from sensor imprecisions or physical limitations, such as aperture effects, motion or atmospheric phenomena. Additionally, a decimation modeled by a sparse or a random matrix can be encountered in several applications: in super-resolution techniques, where the goal is to reconstruct a high resolution multicomponent image from low-resolution ones [4], or in compressive sensing [5] based acquisition systems allowing one to reduce the size of acquired images prior to storage or transmission [6]. As a consequence, the standard imaging model consists of a blurring operator [7] followed by a decimation and a (non-necessarily additive) noise.

The main focus of this paper is multicomponent image recovery from degraded observations, for which it is of paramount importance to exploit the intrinsic correlations along spatial and spectral dimensions. To this end, we adopt a variational approach based on the introduction of a *non-local total variation structure tensor* (ST-NLTV) regularization and we show how to solve it practically with constrained convex optimization techniques.

ST-NLTV regularization: The quality of the results obtained through a variational approach strongly depends on the ability to model the regularity present in images. Since natural images are often piecewise smooth, popular regularization models tend to penalize the image gradient. In this context, *total variation* (TV) [8, 9] has emerged as a simple, yet successful, convex optimization tool. However, TV fails to preserve textures, details and fine structures, because they are hardly distinguishable from noise. To improve this behaviour, the TV model has been extended by using some generalizations based on higher-order spatial differences [10] or a non-locality principle [11, 12, 13]. Another approach to overcome these limitations is to replace the gradient operator with a frame representation which yields a more suitable sparse representation of the image [14, 15, 16, 17, 18, 19]. In this context, the family of Block Matching 3-D (BM3D) algorithms [20, 21] has been recently formulated in terms of analysis and synthesis frames [22], substantiating the use of the non-locality principle as a valuable image modeling tool.

The extension of TV-based models to multicomponent images is, in general, non trivial. A first approach consists of computing TV channel-by-channel and then summing up the resulting smoothness measures [23, 24, 25, 26]. Since there is no coupling of the components, this approach may potentially lead to component smearing and loss of edges across components. An alternative way is to process the components jointly, so as to better reveal

details and features that are not visible in each of the components considered separately. This approach naturally arises when the gradient of a multicomponent image is thought of as a structure tensor [27, 28, 29, 30, 31, 32, 33, 34]. A concise review of both frameworks can be found in [34], where an efficient regularization based on ST-TV was suggested for color imagery.

In order to improve the restoration results obtained in the color and hyperspectral restoration literature based on ST-TV, our first main contribution consists of applying the non-locality principle to ST-TV regularization.

Constrained formulation: Regarding the variational formulation of the data recovery problem, one may prefer to adopt a constrained formulation rather than a regularized one. Indeed, it has been recognized for a long time that incorporating constraints directly on the solution often facilitates the choice of the involved parameters [35, 36, 37, 38, 39, 40], because the constraint bounds are usually related to some physical properties of the target solution or to some knowledge of the degradation process, e.g. the noise statistical properties. One of the difficulties of constrained approaches is however that a closed form of the projection onto the considered constraint set is not always available. Closed forms are known for convex sets such as $\boldsymbol{\ell}_2$-balls, hypercubes defining dynamics range constraints, hyperplanes, or half-spaces [41]. However, more sophisticated constraints are usually necessary in order to effectively restore multicomponent images.

Taking advantage of the flexibility offered by recent proximal algorithms, we propose an epigraphical method allowing us to address a wide class of convex constraints. Our second main contribution is thus to provide an efficient solution based on proximal tools in order to solve convex problems involving matricial $\boldsymbol{\ell}_{1,p}$-ball constraints. The proposed solution avoids the inner iterations that are implemented in the approaches in [42, 43] for solving regression problems.

Imaging spectroscopy: In the context of spectral imagery, one typically distinguishes between *multispectral* (MS) and *hyperspectral* (HS) images. The former ones cover the spectrum from the visible to the infrared, while the latter ones correspond to very narrow band analyses over a contiguous spectral range. For example, a sensor with 20 bands can be either multispectral when it captures 20 bands covering the visible spectrum plus the near/middle/far infrared, or hyperspectral when it captures 20 bands, 10 nm wide each, covering the range from 500 to 700 nm. In general, HS images are capable to achieve a higher spectral resolution than MS images (at the cost of acquiring a few hundred bands), which results in a better spectral characterization of the objects in the scene. This gave rise to a wide array of applications in remote sensing, such as detection and identification of the ground surface [44], as well as military surveillance and historical manuscript research.

The primary characteristics of hyperspectral images is that an entire spectrum is acquired at each point, which implies a huge correlation among close spectral bands. As a result,

there has been an emergence of variational methods to efficiently model the spectral-spatial regularity present in such kind of images. To the best of our knowledge, these methods can be roughly divided into three classes.

A first class of approaches consists of extending the regularity models used in color imagery [34, 45]. To cite a few examples, the work in [4] proposed a super-resolution method based on a component-by-component TV regularization. To deal with the huge size of HS images, the authors performed the actual super-resolution on a few principal image components (obtained by means of PCA), which are then used to interpolate the secondary components. In [18], the problem of MS denoising is dealt with by considering an hybrid regularization that induces each component to be sparse in an orthonormal basis, while promoting similarities between the components by means of a distance function applied on wavelet coefficients. Another kind of spectral adaptivity has been proposed in [46] for HS restoration. It consists of using the multicomponent TV regularization in [32] that averages the Frobenius norms of the multicomponent gradients. The same authors have recently proposed in [47] an inpainting method based on the multicomponent NLTV regularization. The link between this method and the proposed work will be discussed later.

A second class of approaches consists of modeling HS images as three-dimensional tensors, i.e. two spatial dimensions and one spectral dimension. First denoising attempts in this direction were pursued in [48, 49], where tensor algebra was exploited to jointly analyze the HS hypercube considering vectorial anisotropic diffusion methods. Other strategies, based on filtering, consider tensor denoising methods such as multiway Wiener filtering (see [50] for a survey on this subject).

A third class of approaches is based on robust PCA [51] or low-rank and sparse matrix decomposition [52]. These approaches proceed by splitting a HS image into two separate contributions: an image formed by components having similar shapes (low-rank image) and an image that highlights the differences between the components (sparse image). For example, the work in [6] proposed a convex optimization formulation for recovering an HS image from very few compressive-sensing measurements. This approach involved a penalization based on two terms: the $\boldsymbol{\ell}_*$ nuclear norm of the matrix where each column corresponds to the 2D-wavelet coefficients of a spectral band (reshaped in a vector) and the $\boldsymbol{\ell}_{1,2}$-norm of the wavelet-coefficient blocks grouped along the spectral dimension. A similar approach was followed in [53], even though the $\boldsymbol{\ell}_*/\boldsymbol{\ell}_{1,2}$-norm penalization was applied directly on the HS pixels, rather than using a sparsifying linear transform.

A third contribution of this work is to adapt the proposed ST-NLTV regularization in order to efficiently deal with reconstruction problems (not only denoising) in the context of imaging spectroscopy. The resulting strategy is based on tensor algebra ideas but it uses variational strategies rather than anisotropic diffusion or adaptive filtering. Moreover, comparisons with recent works will be performed.

Outline: The paper is organized as follows. Section 2 describes the degradation model and formulates the constrained convex optimization problem based on the non-local structure tensor. Section 3 explains how to minimize the corresponding objective function via proximal tools. Section 4 provides an experimental validation in the context of MS and HS image restoration. Conclusions are given in Section 5.

Notation: Let $\mathcal{H}$ be a real Hilbert space. $\Gamma_0(\mathcal{H})$ denotes the set of proper, lower semicontinuous, convex functions from $\mathcal{H}$ to $]-\infty,+\infty]$. Recall that a function $\varphi\colon \mathcal{H} \to]-\infty,+\infty]$ is proper if its domain $\operatorname{dom}\varphi = \big\{y \in \mathcal{H} \;\big|\; \varphi(y) < +\infty\big\}$ is nonempty. The subdifferential of φ at $x \in \mathcal{H}$ is $\partial\varphi(x) = \big\{u \in \mathcal{H} \;\big|\; (\forall y \in \mathcal{H})\ \langle y - x \mid u\rangle + \varphi(x) \leq \varphi(y)\big\}$. The epigraph of $\varphi \in \Gamma_0(\mathcal{H})$ is the nonempty closed convex subset of $\mathcal{H} \times \mathbb{R}$ defined as $\operatorname{epi}\varphi = \big\{(y,\zeta) \in \mathcal{H} \times \mathbb{R} \;\big|\; \varphi(y) \leq \zeta\big\}$, the lower level set of φ at height $\zeta \in \mathbb{R}$ is the nonempty closed convex subset of $\mathcal{H}$ defined as $\operatorname{lev}_{\leq\zeta}\varphi = \big\{y \in \mathcal{H} \;\big|\; \varphi(y) \leq \zeta\big\}$. The projection onto a nonempty closed convex subset $C \subset \mathcal{H}$ is, for every $y \in \mathcal{H}$, $P_C(y) = \operatorname{argmin}_{u\in C}\|u - y\|$. The indicator function ι_C of C is equal to 0 on C and $+\infty$ otherwise. Finally, Id (resp. Id_N) denotes the identity operator (resp. the identity matrix of size $N \times N$).

2 Proposed approach

2.1 Degradation model

The R-component signal of interest is denoted by $\overline{\mathrm{x}} = (\overline{x}_1, \ldots, \overline{x}_R) \in (\mathbb{R}^N)^R$. In this work, each signal component will generally correspond to an image of size $N = N_1 \times N_2$. In imaging spectroscopy, R denotes the number of spectral bands. The degradation model that we consider in this work is

$$\mathrm{z} = \mathcal{B}(\mathrm{A}\overline{\mathrm{x}}) \tag{1}$$

where $\mathrm{z} = (z_1, \ldots, z_S) \in (\mathbb{R}^K)^S$ denotes the degraded observations, $\mathcal{B}\colon (\mathbb{R}^K)^S \to (\mathbb{R}^K)^S$ models the effect of a (non-necessarily additive) noise, and $\mathrm{A} = (\mathrm{A}_{s,r})_{1\leq s\leq S, 1\leq r\leq R}$ is the degradation linear operator with $\mathrm{A}_{s,r} \in \mathbb{R}^{K\times N}$, for every $(s,r) \in \{1,\ldots,S\} \times \{1,\ldots,R\}$. In particular, this model can be specialized in some of the applications mentioned in the introduction, such as super-resolution and compressive sensing, as well as unmixing as explained in the following.

(i) **Super resolution** (see e.g. [4]). In this scenario, z denotes B multicomponent images at low-resolution and $\overline{\mathrm{x}}$ denotes the (high-resolution) multicomponent image to be recovered. The operator A is a block-diagonal matrix with $S = BR$ while, for every $r \in \{1,\ldots,R\}$ and $b \in \{1,\ldots,B\}$, $\mathrm{A}_{B(r-1)+b,r} = \mathrm{D}_b\mathrm{T}\mathrm{W}_r$ is a composition of a warp matrix $\mathrm{W}_r \in \mathbb{R}^{N\times N}$, a camera blur operator $\mathrm{T} \in \mathbb{R}^{N\times N}$, and a downsampling matrix $\mathrm{D}_b \in \mathbb{R}^{K\times N}$ with $K < N$. The noise is assumed to be a zero-mean white Gaussian

additive noise. It follows that B different noisy decimated versions of the same blurred and warped component are available. This yields the following degradation model: for every $r \in \{1, \dots, R\}$ and $b \in \{1, \dots, B\}$,

$$z_{B(r-1)+b} = \mathrm{D}_b \mathrm{T} \mathrm{W}_r \, \overline{x}_r + \varepsilon_{B(r-1)+b} \tag{2}$$

where $\varepsilon_{B(r-1)+b} \sim \mathcal{N}(0, \sigma^2 \, \mathrm{Id}_K)$.

(ii) **Compressive sensing** (see e.g. [6]). In this scenario, z denotes the *compressed* multicomponent image and $\overline{\mathrm{x}}$ is the multicomponent image to be reconstructed. The operator A is a block-diagonal matrix where $S = R$, for every $r \in \{1, \dots, R\}$, $\mathrm{A}_{r,r} = \mathrm{D}_r$, and $\mathrm{D}_r \in \mathbb{R}^{K \times N}$ is a random measurement matrix with $K \ll N$. The noise is assumed to be a zero-mean white Gaussian additive noise. This leads to the following degradation model:

$$(\forall r \in \{1, \dots, R\}) \qquad z_r = \mathrm{D}_r \, \overline{x}_r + \varepsilon_r \tag{3}$$

where $\varepsilon_r \sim \mathcal{N}(0, \sigma^2 \, \mathrm{Id}_K)$.

(iii) **Unmixing** [54, 55, 56]. In this scenario, z models an HS image with $K = N$ having several components whose spectra, denoted by $(\mathrm{S}_r)_{1 \leq r \leq R} \in (\mathbb{R}^S)^R$, are supposed to be known. The goal is to determine the abundance maps of each component, thus the unknown $\overline{\mathrm{x}}$ models these abundance maps. R denotes the number of components and S the number of spectral measurements. The matrix A has a block diagonal structure that leads to the following mixing model: for every $\ell \in \{1, \dots, N\}$,

$$\begin{bmatrix} z_1^{(\ell)} \\ \vdots \\ z_S^{(\ell)} \end{bmatrix} = \sum_{r=1}^{R} x_r^{(\ell)} \mathrm{S}_r + \varepsilon^{(\ell)}, \tag{4}$$

where $x_r^{(\ell)}$ is the pixel value for the r-th component, $z_s^{(\ell)}$ is the pixel value for the s-th spectral measurement, and $\varepsilon^{(\ell)} \sim \mathcal{N}(0, \sigma^2 \, \mathrm{Id}_S)$ denotes the additive noise. In this work however, we will not focus on hyperspectral unmixing that constitutes a specific application area for which tailored algorithms have been developed.

2.2 Convex optimization problem

A usual solution to recover $\overline{\mathrm{x}}$ from the observations z is to follow a convex variational approach that leads to solving an optimization problem such as

$$\underset{\mathrm{x} \in C}{\text{minimize}} \;\; f(\mathrm{Ax}, \mathrm{z}) \quad \text{s.t.} \quad g(\mathrm{x}) \leq \eta, \tag{5}$$

where $\eta > 0$. The cost function $f(\cdot, \mathrm{z}) \in \Gamma_0\big((\mathbb{R}^K)^S\big)$ aims at insuring that the solution is *close to* the observations. This data term is related to the noise characteristics. For instance,

standard choices for f are a quadratic function for an additive Gaussian noise, an $\boldsymbol{\ell}_1$-norm when a Laplacian noise is involved, and a Kullback-Leibler divergence when dealing with Poisson noise. The function $g \in \Gamma_0\big((\mathbb{R}^N)^R\big)$ allows us to impose some regularity on the solution. Some possible choices for this function have been mentioned in the introduction.

Note that state-of-the-art methods often deal with the regularized version of Problem (5), that is

$$\underset{\mathrm{x}\in C}{\text{minimize}} \;\; f(\mathrm{Ax}, \mathrm{z}) + \lambda g(\mathrm{x}), \tag{6}$$

where $\lambda > 0$. Actually, both formulations are equivalent for some specific values of λ and η. As mentioned in the introduction, the advantage of the constrained formulation is that the choice of η may be easier, since it is directly related to the properties of the signal to be recovered.

Finally, C denotes a nonempty closed convex subset of $(\mathbb{R}^N)^R$, which can be used for purposes like constraining the dynamics range of the signal to be recovered.

2.3 Structure Tensor regularization

In this work, we propose to model the spatial *and* spectral dependencies in multicomponent images by introducing a regularization grounded on the use of a *matrix norm*, which is defined as

$$\big(\forall \mathrm{x} \in (\mathbb{R}^N)^R\big) \qquad g(\mathrm{x}) = \sum_{\ell=1}^{N} \tau_\ell \|\mathrm{F}_\ell \mathrm{B}_\ell \mathrm{x}\|_p, \tag{7}$$

where $\|\cdot\|_p$ denotes the Schatten p-norm with $p \geq 1$, $(\tau_\ell)_{1\leq\ell\leq N}$ are positive weights, and, for every $\ell \in \{1, \ldots, N\}$,

(i) **block selection**: the operator $\mathrm{B}_\ell \colon (\mathbb{R}^N)^R \to \mathbb{R}^{Q^2\times R}$ selects $Q \times Q$ blocks of each component (including the pixel ℓ) and rearranges them in a matrix of size $Q^2 \times R$, so leading to

$$\mathrm{Y}^{(\ell)} = \begin{bmatrix} x_1^{(n_{\ell,1})} & \ldots & x_R^{(n_{\ell,1})} \\ \vdots & & \vdots \\ x_1^{(n_{\ell,Q^2})} & \ldots & x_R^{(n_{\ell,Q^2})} \end{bmatrix} \tag{8}$$

where $\mathcal{W}_\ell = \{n_{\ell,1}, \ldots, n_{\ell,Q^2}\}$ is the set of positions located into the window around ℓ, and $Q > 1$;[1]

(ii) **block transform**: the operator $\mathrm{F}_\ell \colon \mathbb{R}^{Q^2\times R} \to \mathbb{R}^{M_\ell \times R}$ denotes an analysis transform that achieves a sparse representation of grouped blocks, yielding

$$\mathrm{X}^{(\ell)} = \mathrm{F}_\ell \mathrm{Y}^{(\ell)}, \tag{9}$$

[1]The image borders are handled by symmetric extension.

where $M_\ell \leq Q^2$.

The resulting structure tensor regularization reads

$$g(\mathrm{x}) = \sum_{\ell=1}^{N} \tau_\ell \, \|\mathrm{X}^{(\ell)}\|_p. \tag{10}$$

Let us denote by

$$\sigma_{\mathrm{X}^{(\ell)}} = \left(\sigma^{(m)}_{\mathrm{X}^{(\ell)}}\right)_{1 \leq m \leq \widetilde{M}_\ell}, \quad \text{with } \widetilde{M}_\ell = \min\{M_\ell, R\}, \tag{11}$$

the singular values of $\mathrm{X}^{(\ell)}$ ordered in decreasing order. When $p \in [1, +\infty[$, we have

$$g(\mathrm{x}) = \sum_{\ell=1}^{N} \tau_\ell \left(\sum_{m=1}^{\widetilde{M}_\ell} \left(\sigma^{(m)}_{\mathrm{X}^{(\ell)}}\right)^p \right)^{1/p}, \tag{12}$$

whereas, when $p = +\infty$,

$$g(\mathrm{x}) = \sum_{\ell=1}^{N} \tau_\ell \, \sigma^{(1)}_{\mathrm{X}^{(\ell)}}. \tag{13}$$

When $p = 1$, the Schatten norm reduces to the nuclear norm. In such a case, the structure tensor regularization induces a low-rank approximation of matrices $(\mathrm{X}^{(\ell)})_{1 \leq \ell \leq N}$ (see [57] for a survey on singular value decomposition).

The structure tensor regularization proposed in (9) generalizes several state-of-the-art regularization strategies, as explained below.

2.3.1 ST-TV

We retrieve the multicomponent TV regularization [32, 34, 46] by setting F_ℓ to the operator which, for each component index $r \in \{1, \ldots, R\}$, computes the difference between $x_r^{(\ell)}$ and its horizontal/vertical nearest neighbours $(x_r^{(\ell_1)}, x_r^{(\ell_2)})$, yielding the matrix

$$\mathrm{X}^{(\ell)}_{\mathrm{TV}} = \begin{bmatrix} x_1^{(\ell)} - x_1^{(\ell_1)} & \ldots & x_R^{(\ell)} - x_R^{(\ell_1)} \\ x_1^{(\ell)} - x_1^{(\ell_2)} & \ldots & x_R^{(\ell)} - x_R^{(\ell_2)} \end{bmatrix} \tag{14}$$

with $M_\ell = 2$. This implies a 2×2 block selection operator (i.e., $Q = 2$). Note that the regularization proposed in [46] is a special case of this ST-TV constraint arising when $p = 2$. We will refer to it as Hyperspectral-TV in Section 4. Finally, note that the regularization used in [4] is intrinsically different from the ST-TV described above, as the former amounts to summing up the smoothed TV [58] evaluated separately over each component.

2.3.2 ST-NLTV

We extend the NLTV regularization [12] to multicomponent images by setting F_ℓ to the operator which, for each component index $r \in \{1, \ldots, R\}$, computes the weighted difference between $x_r^{(\ell)}$ and some other pixel values. This results in the matrix

$$\mathrm{X}_{\mathrm{NLTV}}^{(\ell)} = \left[\omega_{\ell,n}(x_r^{(\ell)} - x_r^{(n)})\right]_{n\in\mathcal{N}_\ell, 1\leq r\leq R}, \tag{15}$$

where $\mathcal{N}_\ell \subset \mathcal{W}_\ell \setminus \{\ell\}$ denotes the non-local support of the neighbourhood of ℓ. Here, M_ℓ corresponds to the size of this support. Note that the regularization in [47] appears as a special case of the proposed ST-NLTV arising when $p = 2$ and the local window is fully used ($M_\ell = Q^2$). We will refer to it as Multichannel-NLTV in Section 4.

For every $\ell \in \{1, \ldots, N\}$ and $n \in \mathcal{N}_\ell$, the weight $\omega_{\ell,n} > 0$ depends on the similarity between patches built around the pixels ℓ and n of the image to be recovered. Since the degradation process in (1) may involve some missing data, we follow a two-step approach in order to estimate these weights. In the first step, the ST-TV regularization is used in order to obtain an estimate $\widetilde{\mathrm{x}}$ of the target image. This estimate subsequently serves in the second step to compute the weights through a *self-similarity* measure as follows:

$$\omega_{\ell,n} = \widetilde{\omega}_\ell \exp\left(-\delta^{-2}\, \|\mathrm{L}_\ell\widetilde{\mathrm{x}} - \mathrm{L}_n\widetilde{\mathrm{x}}\|_2^2\right), \tag{16}$$

where $\delta > 0$, L_ℓ (resp. L_n) selects a $\widetilde{Q} \times \widetilde{Q} \times R$ patch centered at position ℓ (resp. n) after a linear processing of the image depending on the position ℓ (resp. n), and the constant $\widetilde{\omega}_\ell > 0$ is set so as to normalize the weights (i.e. $\sum_{n\in\mathcal{N}_\ell} \omega_{\ell,n} = 1$). In particular, the operator L_ℓ (resp. L_n) may involve a convolution with either a Gaussian function with mean ℓ (resp. n) and a given variance [11], or a set of low-pass Gaussian filters whose variances increase as the spatial distance from the patch center ℓ (resp. n) grows [59]. For every $\ell \in \{1, \ldots, N\}$, the neighbourhood $\mathcal{N}_\ell$ is built according to the procedure described in [60]. In practice, we limit the size of the neighbourhood, so that $M^{(\ell)} \leq \overline{M}$ (the values chosen for Q, $\widetilde{Q}$, δ and $\overline{M}$ are indicated in Section 4).

3 Optimization method

Within the proposed constrained optimization framework, Problem (5) can be reformulated as follows:

$$\underset{\mathrm{x}\in C}{\text{minimize}}\;\; f(\mathrm{Ax}, \mathrm{z}) \quad \text{s.t.} \quad \Phi\,\mathrm{x} \in D, \tag{17}$$

where Φ is the linear operator defined as

$$\Phi\colon \mathrm{x} \mapsto \mathrm{X} = \begin{bmatrix} \mathrm{F}_1\mathrm{B}_1\mathrm{x} \\ \vdots \\ \mathrm{F}_N\mathrm{B}_N\mathrm{x} \end{bmatrix} \begin{matrix} \} \ \mathrm{X}^{(1)} \\ \\ \} \ \mathrm{X}^{(N)} \end{matrix} \tag{18}$$

with $\mathrm{X} \in \mathbb{R}^{M \times R}$ and $M = M_1 + \cdots + M_N$, while D is the closed convex set defined as

$$D = \big\{ \mathrm{X} \in \mathbb{R}^{M \times R} \;\big|\; \sum_{\ell=1}^{N} \tau_\ell \|\mathrm{X}^{(\ell)}\|_p \leq \eta \big\}. \tag{19}$$

In recent works, iterative procedures were proposed to deal with an $\boldsymbol{\ell}_1$- or $\boldsymbol{\ell}_{1,2}$-ball constraint [42] and an $\boldsymbol{\ell}_{1,\infty}$-ball constraint [43]. Similar techniques can be used to compute the projection onto D, but a more efficient approach consists of adapting the epigraphical splitting technique investigated in [61, 62, 63, 64].

3.1 Epigraphical splitting

Epigraphical splitting applies to a convex set that can be expressed as the lower level set of a separable convex function, such as the constraint set D defined in (19). Some auxiliary variables are introduced into the minimization problem, so that the constraint D can be *equivalently* re-expressed as the intersection of two convex sets. More specifically, different splitting solutions need to be proposed according to the involved Schatten p-norm:

(i) in the case when $p = 1$, since

$$\mathrm{X} \in D \quad \Leftrightarrow \quad \sum_{\ell=1}^{N} \sum_{m=1}^{\widetilde{M}_\ell} \tau_\ell \left| \sigma^{(m)}_{\mathrm{X}^{(\ell)}} \right| \leq \eta, \tag{20}$$

we propose to introduce an auxiliary vector $\zeta \in \mathbb{R}^{\widetilde{M}}$, with $\zeta = (\zeta^{(\ell,m)})_{1 \leq \ell \leq N, 1 \leq m \leq \widetilde{M}_\ell}$ and $\widetilde{M} = \widetilde{M}_1 + \ldots + \widetilde{M}_N$, in order to rewrite (20) as

$$\begin{cases} (\forall \ell \in \{1, \ldots, N\})(\forall m \in \{1, \ldots, \widetilde{M}_\ell\}) \qquad \left| \sigma^{(m)}_{\mathrm{X}^{(\ell)}} \right| \leq \zeta^{(\ell,m)}, \\ \displaystyle\sum_{\ell=1}^{N} \sum_{m=1}^{\widetilde{M}_\ell} \tau_\ell \, \zeta^{(\ell,m)} \leq \eta. \end{cases} \tag{21}$$

Consequently, Constraint (20) is decomposed in two convex sets: a union of epigraphs

$$E = \big\{ (\mathrm{X}, \zeta) \in \mathbb{R}^{M \times R} \times \mathbb{R}^{\widetilde{M}} \;\big|\; (\forall \ell \in \{1, \ldots, N\})(\forall m \in \{1, \ldots, \widetilde{M}_\ell\}) \quad (\sigma^{(m)}_{\mathrm{X}^{(\ell)}}, \zeta^{(\ell,m)}) \in \operatorname{epi} |\cdot| \;\big\}, \tag{22}$$

and the closed half-space

$$W = \big\{ \zeta \in \mathbb{R}^{\widetilde{M}} \;\big|\; \sum_{\ell=1}^{N} \sum_{m=1}^{\widetilde{M}_\ell} \tau_\ell \, \zeta^{(\ell,m)} \leq \eta \big\}. \tag{23}$$

(ii) in the case when $p > 1$, since

$$\mathrm{X} \in D \quad \Leftrightarrow \quad \sum_{\ell=1}^{N} \tau_\ell \, \|\sigma_{\mathrm{X}^{(\ell)}}\|_p \leq \eta, \tag{24}$$

we define an auxiliary vector $\zeta = (\zeta^{(\ell)})_{1 \leq \ell \leq N} \in \mathbb{R}^N$ of *smaller* dimension N, and we rewrite Constraint (24) as

$$\begin{cases} (\forall \ell \in \{1, \dots, N\}) \quad \|\sigma_{\mathrm{X}^{(\ell)}}\|_p \leq \zeta^{(\ell)}, \\ \displaystyle\sum_{\ell=1}^{N} \tau_\ell \, \zeta^{(\ell)} \leq \eta. \end{cases} \tag{25}$$

Similarly to the previous case, Constraint (24) is decomposed in two convex sets: a union of epigraphs

$$E = \big\{(\mathrm{X}, \zeta) \in \mathbb{R}^{M \times R} \ \times \ \mathbb{R}^N \ \big| \ (\forall \ell \in \{1, \dots, N\})(\sigma_{\mathrm{X}^{(\ell)}}, \zeta^{(\ell)}) \in \operatorname{epi} \|\cdot\|_p \big\}, \tag{26}$$

and the closed half-space

$$W = \big\{\zeta \in \mathbb{R}^N \ \big| \ \sum_{\ell=1}^{N} \tau_\ell \, \zeta^{(\ell)} \leq \eta \big\}. \tag{27}$$

3.2 Epigraphical projection

The epigraphical splitting technique allows us to reformulate Problem (17) in a more tractable way, as follows

$$\underset{(\mathrm{x},\zeta) \in C \times W}{\text{minimize}} \ f(\mathrm{Ax}, \mathrm{z}) \quad \text{s.t.} \quad (\Phi \, \mathrm{x}, \, \zeta) \in E. \tag{28}$$

The advantage of such a decomposition is that the projections P_E and P_W onto E and W may have closed-form expressions. Indeed, the projection P_W is well-known [65], while properties of the projection P_E are summarized in the following proposition, which is straightforwardly proved.

Proposition 3.1. *For every $\ell \in \{1, \dots, N\}$, let*

$$\mathrm{X}^{(\ell)} = \mathrm{U}^{(\ell)} \mathrm{S}^{(\ell)} \big(\mathrm{V}^{(\ell)}\big)^\top \tag{29}$$

be the Singular Value Decomposition of $\mathrm{X}^{(\ell)} \in \mathbb{R}^{M_\ell \times R}$, where

- $(\mathrm{U}^{(\ell)})^\top \mathrm{U}^{(\ell)} = \mathrm{Id}_{\widetilde{M}_\ell}$,
- $\big(\mathrm{V}^{(\ell)}\big)^\top \mathrm{V}^{(\ell)} = \mathrm{Id}_{\widetilde{M}_\ell}$,

- $\mathrm{S}^{(\ell)} = \mathrm{Diag}(\mathsf{s}^{(\ell)})$, *with* $\mathsf{s}^{(\ell)} = (\sigma^{(m)}_{\mathrm{X}^{(\ell)}})_{1 \leq m \leq \widetilde{M}_\ell}$.

Then,

$$P_E(\mathrm{X}, \zeta) = \left(\mathrm{U}^{(\ell)} \mathrm{T}^{(\ell)} \left(\mathrm{V}^{(\ell)} \right)^\top, \ \theta^{(\ell)} \right)_{1 \leq \ell \leq N}, \tag{30}$$

where $\mathrm{T}^{(\ell)} = \mathrm{Diag}(\mathsf{t}^{(\ell)})$ *and,*

(i) *in the case* $p = 1$, *for every* $m \in \{1, \ldots, \widetilde{M}_\ell\}$

$$(\mathsf{t}^{(\ell,m)}, \ \theta^{(\ell,m)}) = P_{\mathrm{epi}\,|\cdot|}(\mathsf{s}^{(\ell,m)}, \zeta^{(\ell,m)}), \tag{31}$$

(ii) *in the case* $p > 1$,

$$(\mathsf{t}^{(\ell)}, \ \theta^{(\ell)}) = P_{\mathrm{epi}\,\|\cdot\|_p}(\mathsf{s}^{(\ell)}, \zeta^{(\ell)}). \tag{32}$$

The above result states that the projection onto the epigraph of the $\boldsymbol{\ell}_{1,p}$ matrix norm can be deduced from the projection onto the epigraph of the $\boldsymbol{\ell}_{1,p}$ vector norm. It turns out that closed-form expressions of the latter projection exist when $p \in \{1, 2, +\infty\}$ [61]. For example, for every $(\mathsf{s}^{(\ell)}, \zeta^{(\ell)}) \in \mathbb{R}^{\widetilde{M}_\ell} \times \mathbb{R}$,

$$P_{\mathrm{epi}\,\|\cdot\|_2}(\mathsf{s}^{(\ell)}, \zeta^{(\ell)}) = \begin{cases} (0, 0), & \text{if } \|\mathsf{s}^{(\ell)}\|_2 < -\zeta^{(\ell)}, \\ (\mathsf{s}^{(\ell)}, \zeta^{(\ell)}), & \text{if } \|\mathsf{s}^{(\ell)}\|_2 < \zeta^{(\ell)}, \\ \beta^{(\ell)} \left(\mathsf{s}^{(\ell)}, \|\mathsf{s}^{(\ell)}\|_2 \right), & \text{otherwise}, \end{cases} \tag{33}$$

where $\beta^{(\ell)} = \dfrac{1}{2} \left(1 + \dfrac{\zeta^{(\ell)}}{\|\mathsf{s}^{(\ell)}\|_2} \right)$. Note that the closed-form expression for $p = 1$ can be derived from (33). Moreover,

$$P_{\mathrm{epi}\,\|\cdot\|_\infty}(\mathsf{s}^{(\ell)}, \zeta^{(\ell)}) = (\mathsf{t}^{(\ell)}, \ \theta^{(\ell)}), \tag{34}$$

where, for every $\mathsf{t}^{(\ell)} = (\mathsf{t}^{(\ell,m)})_{1 \leq m \leq \widetilde{M}_\ell} \in \mathbb{R}^{\widetilde{M}_\ell}$,

$$\mathsf{t}^{(\ell,m)} = \min \left\{ \sigma^{(m)}_{X^{(\ell)}}, \theta^{(\ell)} \right\}, \tag{35}$$

$$\theta^{(\ell)} = \frac{\max \left(\zeta^{(\ell)} + \sum_{k=\overline{k}_\ell}^{\widetilde{M}_\ell} \nu^{(\ell,k)}, 0 \right)}{\widetilde{M}_\ell - \overline{k}_\ell + 2}. \tag{36}$$

Hereabove, $(\nu^{(\ell,k)})_{1 \leq k \leq \widetilde{M}_\ell}$ is a sequence of real numbers obtained by sorting $(\sigma^{(m)}_{X^{(\ell)}})_{1 \leq m \leq \widetilde{M}_\ell}$ in ascending order (by setting $\nu^{(\ell,0)} = -\infty$ and $\nu^{(\ell,\widetilde{M}_\ell+1)} = +\infty$), and $\overline{k}_\ell$ is the unique integer in $\{1, \ldots, \widetilde{M}_\ell + 1\}$ such that

$$\nu^{(\ell,\overline{k}_\ell - 1)} < \frac{\zeta^{(\ell)} + \sum_{k=\overline{k}_\ell}^{\widetilde{M}_\ell} \nu^{(\ell,k)}}{\widetilde{M}_\ell - \overline{k}_\ell + 2} \leq \nu^{(\ell,\overline{k}_\ell)} \tag{37}$$

(with the convention $\sum_{k=\widetilde{M}^{(\ell)}+1}^{\widetilde{M}^{(\ell)}} \cdot = 0$).

Note that the computation of the SVD can be avoided when $p = 2$, as the Frobenius norm is equal to the $\boldsymbol{\ell}_2$-norm of the vector of all matrix elements.

3.3 Proposed algorithm

The solution of (28) requires an efficient algorithm for dealing with large scale problems involving nonsmooth functions and linear operators that are non-necessarily circulant. For this reason, we resort here to proximal algorithms [66, 67, 68, 69, 70, 71, 72, 73, 74, 75, 76, 77, 78, 79, 80, 81, 82]. The key tool in these methods is the proximity operator [83] of a function $\phi \in \Gamma_0(\mathcal{H})$ on a real Hilbert space, defined as

$$(\forall \mathrm{u} \in \mathcal{H}) \qquad \mathrm{prox}_{\phi}(\mathrm{u}) = \underset{\mathrm{v} \in \mathcal{H}}{\mathrm{argmin}} \frac{1}{2}\|\mathrm{v} - \mathrm{u}\|^2 + \phi(\mathrm{v}). \tag{38}$$

The proximity operator can be interpreted as an implicit subgradient step for the function ϕ, since $\mathrm{p} = \mathrm{prox}_{\phi}(\mathrm{u})$ is uniquely defined through the inclusion $\mathrm{u} - \mathrm{p} \in \partial\phi(\mathrm{p})$. Proximity operators enjoy many interesting properties [67]. In particular, they generalize the notion of projection onto a closed convex set C, in the sense that $\mathrm{prox}_{\iota_C} = P_C$. Hence, proximal methods provide a unifying framework that allows one to address a wide class of convex optimization problems involving non-smooth penalizations and hard constraints.

Among the wide array of existing proximal algorithms, we employ the primal-dual M+LFBF algorithm recently proposed in [79], which is able to address general convex optimization problems involving nonsmooth functions and linear operators without requiring any matrix inversion. This algorithm is able to solve numerically:

$$\underset{\mathrm{v} \in \mathcal{H}}{\text{minimize}} \;\; \phi(\mathrm{v}) + \sum_{i=1}^{I} \psi_i(\mathrm{T}_i \mathrm{v}) + \varphi(\mathrm{v}). \tag{39}$$

where $\phi \in \Gamma_0(\mathcal{H})$, for every $i \in \{1, \ldots, I\}$, $\mathrm{T}_i \colon \mathcal{H} \to \mathcal{G}_i$ is a bounded linear operator, $\psi_i \in \Gamma_0(\mathcal{G}_i)$ and $\varphi \colon \mathcal{H} \to \left]-\infty, +\infty\right]$ is a convex differentiable function with a μ-Lipschitzian gradient. Our minimization problem fits nicely into this framework by setting $\mathcal{H} = (\mathbb{R}^N)^R \times \mathbb{R}^L$ with

$$L = \begin{cases} \widetilde{M} & \text{if } p = 1, \\ N & \text{if } p > 1, \end{cases} \tag{40}$$

and $\mathrm{v} = (\mathrm{x}, \zeta)$. Indeed, we set $I = 2$, $\mathcal{G}_1 = \mathbb{R}^{M \times R} \times \mathbb{R}^L$ and $\mathcal{G}_2 = (\mathbb{R}^K)^S$ in (39), the linear operators reduce to

$$\mathrm{T}_1 = \begin{bmatrix} \Phi & 0 \\ 0 & \mathrm{Id}_L \end{bmatrix}, \qquad \mathrm{T}_2 = \begin{bmatrix} \mathrm{A} & 0 \end{bmatrix}, \tag{41}$$

and the functions are as follows

$$\begin{array}{lll}
(\forall(\mathrm{x},\zeta)\in(\mathbb{R}^N)^R\times\mathbb{R}^L) & \phi(\mathrm{x},\zeta) & =\iota_C(\mathrm{x})+\iota_W(\zeta),\\
(\forall(\mathrm{x},\zeta)\in(\mathbb{R}^N)^R\times\mathbb{R}^L) & \phi(\mathrm{x},\zeta) & =\iota_C(\mathrm{x})+\iota_W(\zeta),\\
(\forall(\mathrm{X},\zeta)\in\mathbb{R}^{M\times R}\times\mathbb{R}^L) & \psi_1(\mathrm{X},\zeta) & =\iota_E(\mathrm{X},\zeta),\\
(\forall\mathrm{y}\in(\mathbb{R}^K)^S) & \psi_2(\mathrm{y}) & =f(\mathrm{y},\mathrm{z}),\\
(\forall(\mathrm{x},\zeta)\in(\mathbb{R}^N)^R\times\mathbb{R}^L) & \varphi(\mathrm{x},\zeta) & =0.
\end{array} \tag{42}$$

The iterations associated with Problem (28) are summarized in Algorithm 1, where $\mathrm{A}^\top$ and $\Phi^\top$ designate the adjoint operators of A and Φ. The sequence $(\mathrm{x}^{[t]})_{t\in\mathbb{N}}$ generated by the algorithm is guaranteed to converge to a solution to (28) (see [79]).

Algorithm 1 M+LFBF for solving Problem (28)

Initialization

$\mathrm{Y}_1^{[0]}\in\mathbb{R}^{M\times R},\nu_1^{[0]}\in\mathbb{R}^L$

$\mathrm{y}_2^{[0]}\in(\mathbb{R}^K)^S$

$\mathrm{x}^{[0]}\in(\mathbb{R}^N)^R,\zeta^{[0]}\in\mathbb{R}^L$

$\theta=\sqrt{\|\mathrm{A}\|^2+\max\{\|\Phi\|^2,1\}}$

$\epsilon\in]0,\frac{1}{\theta+1}[$

For $t=0,1,\ldots$

$\gamma_t\in\left[\epsilon,\dfrac{1-\epsilon}{\theta}\right]$

$\left(\widehat{\mathrm{x}}^{[t]},\widehat{\zeta}^{[t]}\right)=\left(\mathrm{x}^{[t]},\zeta^{[t]}\right)-\gamma_t\left(\Phi^\top\mathrm{Y}_1^{[t]}+\mathrm{A}^\top\mathrm{y}_2^{[t]},\nu^{[t]}\right)$

$\left(\mathrm{p}^{[t]},\rho^{[t]}\right)=\left(P_C(\widehat{\mathrm{x}}^{[t]}),P_W(\widehat{\zeta}^{[t]})\right)$

$\left(\widehat{\mathrm{Y}}_1^{[t]},\widehat{\nu}_1^{[t]}\right)=\left(\mathrm{Y}_1^{[t]},\nu_1^{[t]}\right)+\gamma_t\left(\Phi\mathrm{x}^{[t]},\zeta^{[t]}\right)$

$\left(\widetilde{\mathrm{Y}}_1^{[t]},\widetilde{\nu}_1^{[t]}\right)=\left(\widehat{\mathrm{Y}}_1^{[t]},\widehat{\nu}_1^{[t]}\right)-\gamma_t P_E\left(\widehat{\mathrm{Y}}_1^{[t]}/\gamma_t,\widehat{\nu}_1^{[t]}/\gamma_t\right)$

$\left(\mathrm{Y}_1^{[t+1]},\nu_1^{[t+1]}\right)=\left(\widetilde{\mathrm{Y}}_1^{[t]},\widetilde{\nu}_1^{[t]}\right)+\gamma_t\left(\Phi(\mathrm{p}^{[t]}-\mathrm{x}^{[t]}),\rho^{[t]}-\zeta^{[t]}\right)$

$\widehat{\mathrm{y}}_2^{[t]}=\mathrm{y}_2^{[t]}+\gamma_t\mathrm{A}\mathrm{x}^{[t]}$

$\widetilde{\mathrm{y}}_2^{[t]}=\widehat{\mathrm{y}}_2^{[t]}-\gamma_t\,\mathrm{prox}_{\gamma_t^{-1}f}\left(\widehat{\mathrm{y}}_2^{[t]}/\gamma_t\right)$

$\mathrm{y}_2^{[t+1]}=\widetilde{\mathrm{y}}_2^{[t]}+\gamma_t\mathrm{A}(\mathrm{p}^{[t]}-\mathrm{x}^{[t]})$

$\left(\widetilde{\mathrm{x}}^{[t]},\widetilde{\zeta}^{[t]}\right)=\left(\mathrm{p}^{[t]},\rho^{[t]}\right)-\gamma_t\left(\Phi^\top\widetilde{\mathrm{Y}}_1^{[t]}+\mathrm{A}^\top\widetilde{\mathrm{y}}_2^{[t]},\widetilde{\nu}_1^{[t]}\right)$

$\left(\mathrm{x}^{[t+1]},\zeta^{[t+1]}\right)=\left(\mathrm{x}^{[t]}-\widehat{\mathrm{x}}^{[t]}+\widetilde{\mathrm{x}}^{[t]},\zeta^{[t]}-\widehat{\zeta}^{[t]}+\widetilde{\zeta}^{[t]}\right)$

3.4 Approach based on ADMM

Note that an alternative approach to deal with Problem (17) consists of employing the Alternating Direction Method of Multipliers (ADMM) [84] or one of its parallel versions

[73,74,85,86,87,88], sometimes referred to as the Simultaneous Direction Method of Multipliers (SDMM). Although these algorithms are appealing, they require to invert the operator $\mathrm{Id} + \Phi^\top \Phi + \mathrm{A}^\top \mathrm{A}$, which makes them less attractive than primal-dual algorithms for solving Problem (17). Indeed, this matrix is not diagonalizable in the DFT domain (due to the form of Φ), which rules out efficient inversion techniques such as those employed in [86, 89, 90]. To the best of our knowledge, this issue can be circumvented in specific cases only, for example when Φ denotes the NLTV operator defined in (15). In this case, one may resort to the solution in [18, 91], which consists of decomposing Φ as follows:

$$\Phi = \Omega \underbrace{\begin{bmatrix} \mathrm{G}_1 \\ \vdots \\ \mathrm{G}_{Q^2-1} \end{bmatrix}}_{\mathrm{G}}, \tag{43}$$

where, for every $q \in \{1, \ldots, Q^2 - 1\}$, $\mathrm{G}_q \colon (\mathbb{R}^N)^R \to \mathbb{R}^{N \times R}$ is a discrete difference operator and $\Omega \in \mathbb{R}^{M \times N(Q^2-1)}$ is a weighted block-selection operator. Consequently, Problem (17) can be *equivalently* reformulated by introducing an auxiliary variable $\xi = \Phi \mathrm{x} \in \mathbb{R}^{M \times R}$ in the minimization problem, yielding

$$\underset{(\mathrm{x},\xi) \in C \times D}{\text{minimize}} \; f(\mathrm{Ax}, \mathrm{z}) \quad \text{s. t.} \quad (\mathrm{Gx}, \xi) \in V, \tag{44}$$

where $V = \big\{(\mathrm{X}, \xi) \in \mathbb{R}^{N(Q^2-1) \times R} \times \mathbb{R}^{M \times R} \;\big|\; \Omega \mathrm{X} = \xi\big\}$. The iterations associated to SDMM are illustrated in Algorithm 2.

It is worth emphasizing that SDMM still requires to compute the projection onto D, which may be done by either resorting to specific numerical solutions [42, 43, 92, 93] or employing the epigraphical splitting technique presented in Section 3.1. However, according to our simulations (see Section 4.1), both approaches are slower than Algorithm 1.

4 Numerical results

In this section, we numerically evaluate the ST-NLTV regularization proposed in Section 2 and compare Algorithm 1 with implementations of two state-of-the-art methods:

- Hyperspectral TV (H-TV) [46] – see Section 2.3.1,
- Multichannel NLTV (M-NLTV) [47] – see Section 2.3.2.

To this end, two scenarios are addressed: a compressive sensing scenario by using the degradation model (3) where the measurement operator reduces to a random decimation,

Algorithm 2 SDMM for solving Problem (44)

Initialization

$\mathrm{y}_1^{[0]} \in (\mathbb{R}^N)^R, \mathrm{Y}_2^{[0]} \in \mathbb{R}^{M\times R}, \mathrm{y}_3^{[0]} \in (\mathbb{R}^K)^S$

$\overline{\mathrm{y}}_1^{[0]} \in (\mathbb{R}^N)^R, \overline{\mathrm{Y}}_2^{[0]} \in \mathbb{R}^{M\times R}, \overline{\mathrm{y}}_3^{[0]} \in (\mathbb{R}^K)^S$

$\chi_1^{[0]} \in \mathbb{R}^{M\times R}, \chi_2^{[0]} \in \mathbb{R}^{M\times R}$

$\overline{\chi}_1^{[0]} \in \mathbb{R}^{M\times R}, \overline{\chi}_2^{[0]} \in \mathbb{R}^{M\times R}$

$\mathrm{H} = \mathrm{Id} + \mathrm{G}^\top\mathrm{G} + \mathrm{A}^\top\mathrm{A}$

For $t = 0, 1, \ldots$

$\gamma_t \in]0, +\infty[$

$\mathrm{x}^{[t]} = \mathrm{H}^{-1}\left[\mathrm{y}_1^{[t]} - \overline{\mathrm{y}}_1^{[t]} + \mathrm{G}^\top(\mathrm{Y}_2^{[t]} - \overline{\mathrm{Y}}_2^{[t]}) + \mathrm{A}^\top(\mathrm{y}_3^{[t]} - \overline{\mathrm{y}}_3^{[t]})\right]$

$\xi^{[t]} = \frac{1}{2}\left(\chi_1^{[t]} - \overline{\chi}_1^{[t]}\right) + \frac{1}{2}\left(\chi_2^{[t]} - \overline{\chi}_2^{[t]}\right)$

$\mathrm{y}_1^{[t+1]} = P_C\left(\mathrm{x}^{[t]} + \overline{\mathrm{y}}_1^{[t]}\right)$

$\chi_1^{[t+1]} = P_D\left(\xi^{[t]} + \overline{\chi}_1^{[t]}\right)$

$\left(\mathrm{Y}_2^{[t+1]}, \chi_2^{[t+1]}\right) = P_V(\mathrm{Gx}^{[t]} + \overline{\mathrm{Y}}_2^{[t]}, \xi^{[t]} + \overline{\chi}_2^{[t]})$

$\mathrm{y}_3^{[t+1]} = \mathrm{prox}_{\gamma_t f}\left(\mathrm{Ax}^{[t]} + \overline{\mathrm{y}}_3^{[t]}\right)$

$\overline{\mathrm{y}}_1^{[t+1]} = \overline{\mathrm{y}}_1^{[t]} + \mathrm{x}^{[t]} - \mathrm{y}_1^{[t+1]}$

$\overline{\chi}_1^{[t+1]} = \overline{\chi}_1^{[t]} + \xi^{[t]} - \chi_1^{[t+1]}$

$\overline{\mathrm{Y}}_2^{[t+1]} = \overline{\mathrm{Y}}_2^{[t]} + \mathrm{Gx}^{[t]} - \mathrm{Y}_2^{[t+1]}$

$\overline{\chi}_2^{[t+1]} = \overline{\chi}_2^{[t]} + \xi^{[t]} - \chi_2^{[t+1]}$

$\overline{\mathrm{y}}_3^{[t+1]} = \overline{\mathrm{y}}_3^{[t]} + \mathrm{Ax}^{[t]} - \mathrm{y}_3^{[t+1]}$

and a restoration scenario by replacing the measurement operator in (3) with a decimated convolution. For reproducibility purposes, we use several publicly available multispectral and hyperspectral images.[2] The SNR index is used to give a quantitative assessment of the results of the simulated experiments. In particular, we report the SNR computed over all the image components and the *mean* SNR (M-SNR) computed by averaging the SNR evaluated component-by-component.

In our experiments, the images are degraded by (spectrally independent) additive zero-mean white Gaussian noises. Before degrading the original images, the pixels of each component are normalized between $[0, 255]$. Therefore, the fidelity term related to the noise neg-log-likelihood is $f = \|A \cdot -z\|_2^2$ and the dynamics range constraint set C imposes that the pixel values belong to $[0, 255]$. For the ST constraints, we set $Q = 11$, $\widetilde{Q} = 5$, $\delta = 35$ and $\overline{M} = 14$, as this setting was observed to yield the best numerical results.

Extensive tests have been carried out on several images of different sizes. The SNR and M-SNR indices obtained by using the proposed $\boldsymbol{\ell}_1$-ST-TV and $\boldsymbol{\ell}_1$-ST-NLTV regularization

[2] https://engineering.purdue.edu/∼biehl/MultiSpec/hyperspectral.html

constraints are collected in Tables 1 and 2 for the two degradation scenarios mentioned above. In addition, a comparison is performed between our method and the H-TV and M-NLTV algorithms mentioned above (using an M+LFBF implementation). The hyper-parameter for each method (the bound η for the ST constraint in our algorithm) was hand-tuned in order to achieve the best SNR values. The best results are highlighted in bold. Moreover, a component-by-component comparison of two hyperspectral images is made in Figure 2, while a visual comparison of a component from the image *hydice* is displayed in Figure 1.

The aforementioned results demonstrate the interest of combining the non-locality principle with structure-tensor smoothness measures. Indeed, $\boldsymbol{\ell}_1$-ST-NLTV proves to be the most effective regularization with gains in SNR (up to 1.4 dB) with respect to M-NLTV, which in turn is comparable with $\boldsymbol{\ell}_1$-ST-TV. The better performance of $\boldsymbol{\ell}_1$-ST-NLTV seems to be related to its ability to better preserve edges and thin structures present in images, while preventing component smearing.

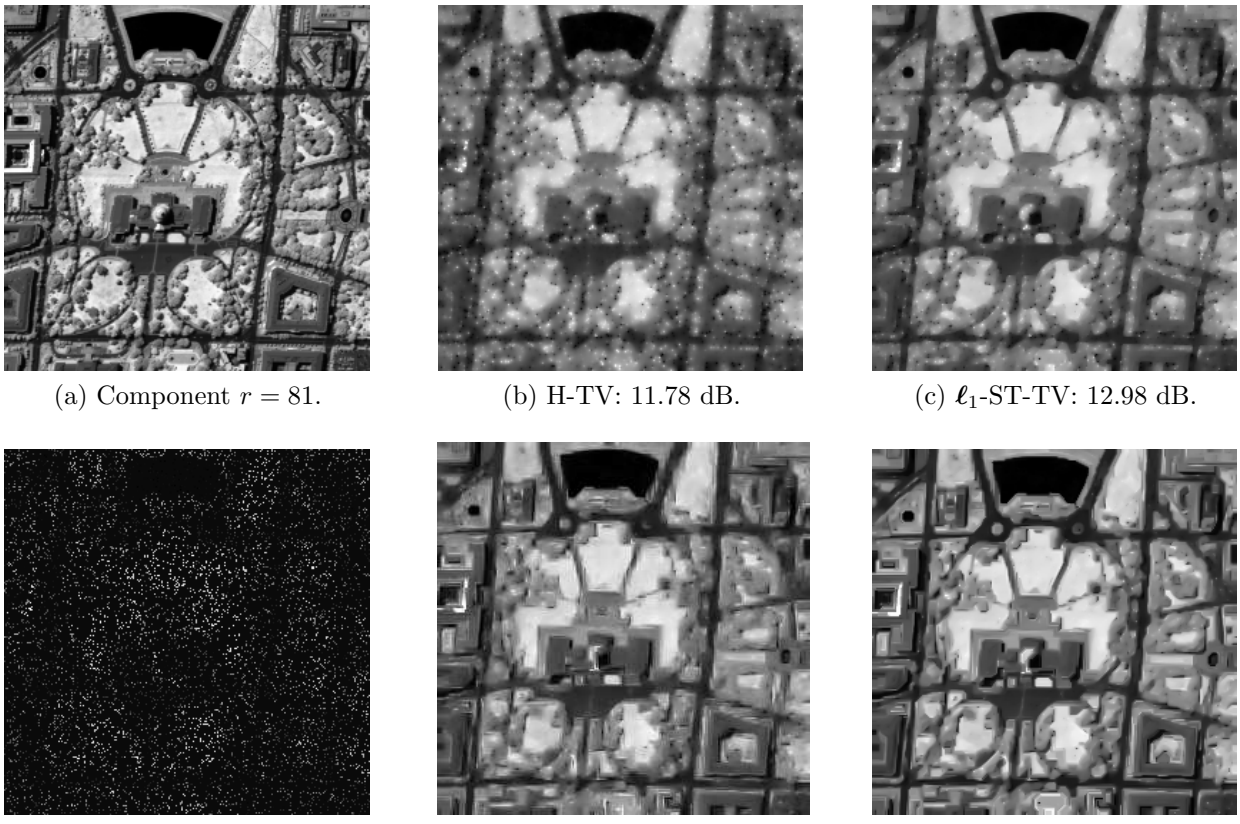

(a) Component $r = 81$. (b) H-TV: 11.78 dB. (c) $\boldsymbol{\ell}_1$-ST-TV: 12.98 dB.

(d) Noisy. (e) M-NLTV: 12.76 dB. (f) **$\boldsymbol{\ell}_1$-ST-NLTV: 14.36 dB**.

Figure 1: Visual comparison of the hyperspectral image *hydice* reconstructed with H-TV [46], $\boldsymbol{\ell}_1$-ST-TV, M-NLTV [47] and $\boldsymbol{\ell}_1$-ST-NLTV. Degradation: compressive sensing scenario involving an additive zero-mean white Gaussian noise with std. deviation 5 and 90% of decimation ($N = 65536$, $R = 191$, $K = 6553$ and $S = 191$).

Table 1: SNR (dB) – Mean SNR (dB) of reconstructed images (Degradation: std. deviation = 5, decimation = 90%).

image	size	H-TV [46]	ℓ_1-ST-TV	M-NLTV [47]	ℓ_1-ST-NLTV
Hydice	$256 \times 256 \times 191$	10.65 – 09.87	11.93 – 11.16	11.57 – 10.76	**12.98 – 12.11**
Indian Pine	$145 \times 145 \times 200$	17.31 – 17.00	18.46 – 18.24	17.62 – 17.34	**19.53 – 19.49**
Little Coriver	$512 \times 512 \times 7$	17.81 – 18.20	18.49 – 18.83	18.46 – 18.90	**19.88 – 20.18**
Mississippi	$512 \times 512 \times 7$	18.27 – 18.07	18.60 – 18.37	18.94 – 18.59	**19.56 – 19.28**
Montana	$512 \times 512 \times 7$	22.49 – 20.97	22.68 – 21.15	22.85 – 21.29	**23.31 – 21.76**
Rio	$512 \times 512 \times 7$	16.48 – 15.29	16.65 – 15.48	16.82 – 15.64	**17.20 – 16.05**
Paris	$512 \times 512 \times 7$	14.85 – 14.31	14.94 – 14.39	15.05 – 14.53	**15.36 – 14.82**

Table 2: SNR (dB) – mean SNR (dB) of restored images (Degradation: std. deviation = 5, blur = 5×5, decimation = 70%).

image	size	H-TV [46]	ℓ_1-ST-TV	M-NLTV [47]	ℓ_1-ST-NLTV
Hydice	$256 \times 256 \times 191$	13.76 – 12.90	14.30 – 13.50	13.84 – 12.98	**14.84 – 14.08**
Indian Pine	$145 \times 145 \times 200$	19.80 – 19.65	20.22 – 20.13	19.73 – 19.57	**20.43 – 20.41**
Little Coriver	$512 \times 512 \times 7$	21.35 – 21.88	21.62 – 22.01	21.31 – 22.00	**21.99 – 22.49**
Mississippi	$512 \times 512 \times 7$	21.12 – 20.29	21.21 – 20.27	21.41 – 20.52	**21.65 – 20.83**
Montana	$512 \times 512 \times 7$	24.80 – 23.37	24.82 – 23.31	24.96 – 23.53	**25.18 – 23.72**
Rio	$512 \times 512 \times 7$	18.62 – 17.50	18.57 – 17.48	18.57 – 17.60	**18.87 – 17.80**
Paris	$512 \times 512 \times 7$	16.68 – 16.55	16.80 – 16.53	16.73 – 16.60	**17.05 – 16.81**

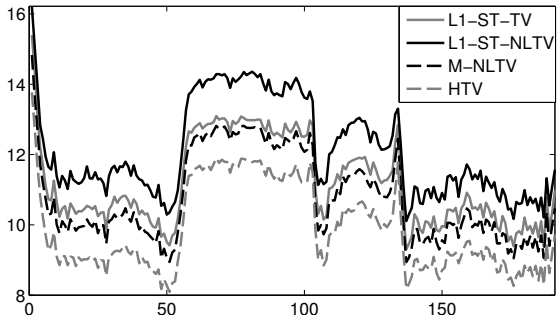

(a) SNR (dB) vs component index (image: hydice).

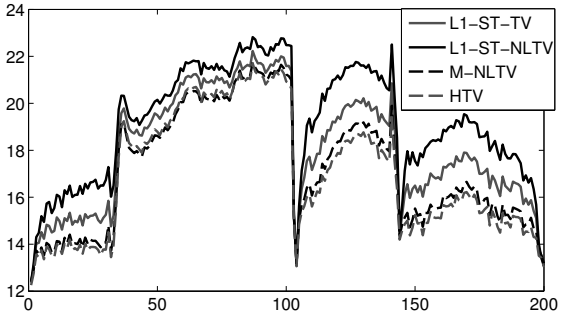

(b) SNR (dB) vs component index (image: indian pine).

Figure 2: Quantitative comparison of two hyperspectral images reconstructed with H-TV [46], ℓ_1-ST-TV, M-NLTV [47] and ℓ_1-ST-NLTV. Degradation: compressive sensing scenario involving an additive zero-mean white Gaussian noise with std. deviation 5 and 90% of decimation.

4.1 Comparison with SDMM

To complete our analysis, we compare the execution time of Algorithm 1 with respect to three alternative solutions:

- M+LFBF applied to Problem (17) by computing the projection onto D via the iterative procedure in [42];
- SDMM applied to Problem (44) by computing the projection onto D via the iterative procedure in [42] (Algorithm 2);
- SDMM applied to Problem (44) after that D is replaced by the constraints E and W.

We would like to emphasize that all the aforementioned algorithms solve *exactly* Problem (17), hence they produce equivalent results (i.e. they converge to the same solution). Our objective here is to empirically demonstrate that the epigraphical splitting technique and primal-dual proximal algorithms constitute a competitive choice for the problem at hand.

We present the results obtained with the image *indian pine*, since a similar behaviour was observed for other images. The stopping criterion is set to $\|x^{[i+1]} - x^{[i]}\| \leq 10^{-5}\|x^{[i]}\|$. Our codes were developed in MATLAB R2011b (the operators Φ and $\Phi^\top$ being implemented in C using mex files) and executed on an Intel Xeon CPU at 2.80 GHz and 8 GB of RAM. For the $\boldsymbol{\ell}_1$-ball projectors needed by the direct method to compute the projection onto D, we used the software publicly available on-line (at `www.cs.ubc.ca/~mpf/spgl1`) [42].

Fig. 3 shows the relative error $\|x^{[i]} - x^{[\infty]}\|/\|x^{[\infty]}\|$ as a function of the computational time, where $x^{[\infty]}$ denotes the solution computed with a stopping criterion of 10^{-5}. These plots indicate that the epigraphical approach yields a faster convergence than the direct one for both SDMM and M+LFBF, the latter being much faster than the former. This can be explained by the computational cost of the subiterations required by the direct projection onto the $\boldsymbol{\ell}_1$-ball. Note that these conclusions extend to all images in the dataset.

The results in Fig. 3 refer to the constraint bound η that achieves the best SNR indices. In practice, the optimal bound may not be known precisely. Although it is out of the scope of this paper to devise an optimal strategy to set this bound, it is important to evaluate the impact of its choice on our method performance. In Tables 3 and 4, we compare the epigraphical approach with the direct computation of the projections (via standard iterative solutions) for different choices of η. For better readability, the values of η are expressed as a multiplicative factor of the ST-TV and ST-NLTV semi-norms of the original image. The execution times indicate that the epigraphical approach yields a faster convergence than the direct approach for SDMM and M+LFBF. Moreover, the numerical results show that errors within $\pm 10\%$ from the optimal value for η lead to SNR variations within 2.6%. We refer to [61] for an extensive comparison between the epigraphical approach and the direct computation of the projections.

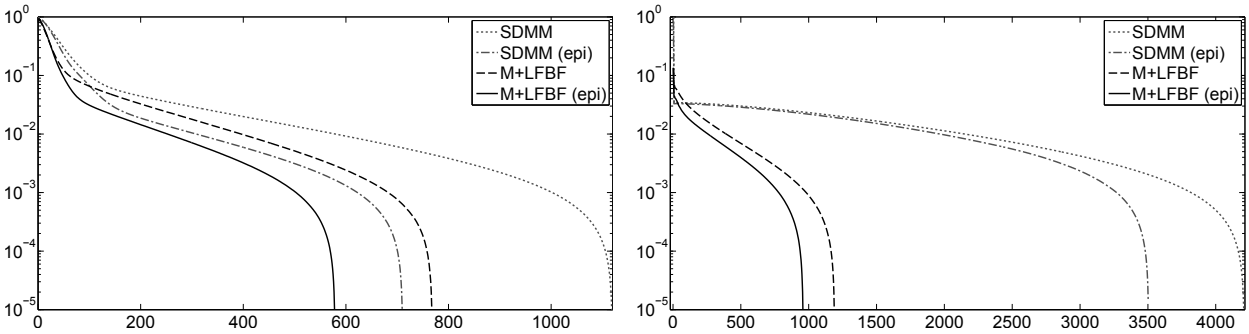

(a) ℓ_1-ST-TV. (b) ℓ_1-ST-NLTV.

Figure 3: Comparison between epigraphical and direct methods: $\frac{\|x^{[i]}-x^{[\infty]}\|}{\|x^{[\infty]}\|}$ vs time (Degradation: std. deviation = 5, decimation = 90%).

Table 3: Results for the ℓ_1-ST-TV constraint and some values of η (Degradation: std. deviation = 5, decimation = 90%)

η	SNR (dB) – M-SNR (dB)	SDMM					M+LFBF				
		direct		epigraphical		speed up	direct		epigraphical		speed up
		# iter.	sec.	# iter.	sec.		# iter.	sec.	# iter.	sec.	
0.3	18.28 – 18.05	394	499.97	377	378.38	1.32	327	333.18	281	252.38	1.32
0.4	**18.46 – 18.24**	**838**	**1066.24**	**698**	**701.03**	**1.52**	**733**	**735.36**	**621**	**558.37**	**1.32**
0.5	16.48 – 16.10	647	830.14	173	173.72	4.78	523	528.39	138	124.07	4.25

Table 4: Results for the ℓ_1-ST-NLTV constraint and some values of η (Degradation: std. deviation = 5, decimation = 90%)

η	SNR (dB) – M-SNR (dB)	SDMM					M+LFBF				
		direct		epigraphical		speed up	direct		epigraphical		speed up
		# iter.	sec.	# iter.	sec.		# iter.	sec.	# iter.	sec.	
		Neighbourhood size: $Q = 3$									
0.2	18.94 – 18.82	1000	4390.05	1000	3421.04	1.28	170	452.78	180	411.28	1.10
0.3	19.39 – 19.32	1000	4414.94	1000	3417.18	1.29	243	649.31	236	534.50	1.21
0.4	19.30 – 19.22	941	4186.20	1000	3441.78	1.22	445	1190.30	442	957.63	1.24
		Neighbourhood size: $Q = 5$									
0.2	19.21 – 19.14	1000	15595.51	1000	11298.05	1.38	171	777.38	171	711.63	1.09
0.3	**19.53 – 19.49**	**1000**	**15338.36**	**1000**	**11174.68**	**1.37**	**275**	**1257.71**	**268**	**1143.35**	**1.10**
0.4	19.33 – 19.25	1000	15403.72	1000	11442.47	1.35	500	2285.51	479	2043.51	1.12

5 Conclusions

We have proposed a new regularization for multicomponent images that is a combination of *non-local total variation* and *structure tensor*. The resulting image recovery problem has been formulated as a constrained convex optimization problem and solved through a novel epigraphical projection method using primal-dual proximal algorithms. The obtained results demonstrate the better performance of structure tensor and non-local gradients over a number of multispectral and hyperspectral images. Our results also show that the nuclear norm has to be preferred over the Frobenius norm for hyperspectral image recovery problems. Furthermore, the experimental part indicates that the epigraphical method converges faster than the approach based on the direct computation of the projections via standard iterative solutions. In both cases, the proposed algorithm turns out to be faster than solutions based on the Alternating Direction Method of Multipliers, suggesting that primal-dual proximal algorithms constitute a good choice in practice to deal with multicomponent image recovery problems.

References

[1] P. Valero, S. Salembier and J. Chanussot, "Hyperspectral image representation and processing with binary partition trees," *IEEE Trans. Image Process.*, vol. 22, no. 4, pp. 1430–1443, Apr. 2013.

[2] R. Molina, J. Nunez, F. J. Cortijo, and J. Mateos, "Image restoration in astronomy: A Bayesian perspective," *IEEE Signal Proc. Mag.*, vol. 18, no. 2, pp. 11–29, Mar. 2001.

[3] C. Vonesch, F. Aguet, J.-L. Vonesch, and M. Unser, "The colored revolution of bioimaging," *IEEE Signal Proc. Mag.*, vol. 23, no. 3, pp. 20–31, May 2006.

[4] H. Zhang, L. Zhang, and H. Shen, "A super-resolution reconstruction algorithm for hyperspectral images," *Elsevier Sig. Proc.*, vol. 92, no. 9, pp. 2082–2096, Sept. 2012.

[5] H. Rauhut, K. Schnass, and P. Vandergheynst, "Compressed sensing and redundant dictionaries," *IEEE Trans. Inform. Theory*, vol. 54, no. 5, pp. 2210–2219, May 2008.

[6] M. Golbabaee and P. Vandergheynst, "Hyperspectral image compressed sensing via low-rank and joint-sparse matrix recovery," in *Proc. Int. Conf. Acoust., Speech Signal Process.*, Kyoto, Japan, Mar. 2012.

[7] J. Oliveira, M.A.T. Figueiredo, and J. Bioucas-Dias, "Parametric blur estimation for blind restoration of natural images: linear motion and out-of-focus," *IEEE Trans. Image Process.*, vol. 23, pp. 466–477, 2014.

[8] L. Rudin, S. Osher, and E. Fatemi, "Nonlinear total variation based noise removal algorithms," *Physica D*, vol. 60, no. 1-4, pp. 259–268, Nov. 1992.

[9] P. L. Combettes and J.-C. Pesquet, "Image restoration subject to a total variation constraint," *IEEE Trans. Image Process.*, vol. 13, no. 9, pp. 1213–1222, Sept. 2004.

[10] K. Bredies, K. Kunisch, and T. Pock, "Total generalized variation," *SIAM J. on Imaging Sci.*, vol. 3, no. 3, pp. 492–526, Sept. 2010.

[11] A. Buades, B. Coll, and J. Morel, "A review of image denoising algorithms, with a new one," *Multiscale Model. and Simul.*, vol. 4, no. 2, pp. 490–530, 2005.

[12] G. Gilboa and S. Osher, "Nonlocal operators with applications to image processing," *Multiscale Model. and Simul.*, vol. 7, no. 3, pp. 1005, 2009.

[13] V. Duval, J.-F. Aujol, and Y. Gousseau, "A bias-variance approach for the non-local means," *SIAM J. on Imaging Sci.*, vol. 4, no. 2, pp. 760–788, 2011.

[14] S. Mallat, *A wavelet tour of signal processing*, Academic Press, San Diego, USA, 1997.

[15] A. Benazza-Benyahia and J.-C. Pesquet, "Building robust wavelet estimators for multicomponent images using Stein's principle," *IEEE Trans. Image Process.*, vol. 14, no. 11, pp. 1814 – 1830, 2005.

[16] C. Chaux, L. Duval, A. Benazza-Benyahia, and J.-C. Pesquet, "A nonlinear Stein-based estimator for multichannel image denoising," *IEEE Trans. Signal Process.*, vol. 56, no. 8, pp. 3855 – 3870, 2008.

[17] C. Chaux, A. Benazza-Benyahia, J.-C. Pesquet, and Duval, "Wavelet transform for the denoising of multivariate images," pp. 203–237. ISTE Ltd and John Wiley & Sons Inc, 2010.

[18] L. M. Briceño-Arias, P. L. Combettes, J.-C. Pesquet, and N. Pustelnik, "Proximal algorithms for multicomponent image recovery problems," *J. Math. Imag. Vis.*, vol. 41, no. 1, pp. 3–22, Sept. 2011.

[19] A. Foi, V. Katkovnik, and K. Egiazarian, "Pointwise shape-adaptive DCT for high-quality denoising and deblocking of grayscale and color images," *IEEE Trans. Image Process.*, vol. 16, no. 5, pp. 1395 – 1411, May 2007.

[20] K. Dabov, A. Foi, V. Katkovnik, and K. Egiazarian, "Image denoising by sparse 3D transform-domain collaborative filtering," *IEEE Trans. Image Process.*, vol. 16, no. 8, pp. 2080 – 2095, Aug. 2007.

[21] M. Maggioni, V. Katkovnik, K. Egiazarian, and A. Foi, "A nonlocal transform-domain filter for volumetric data denoising and reconstruction," *IEEE Trans. Image Process.*, vol. 22, no. 1, pp. 119 – 133, Jan. 2013.

[22] A. Danielyan, V. Katkovnik, and K. Egiazarian, "BM3D frames and variational image deblurring," *IEEE Trans. Image Process.*, vol. 21, no. 4, pp. 1715–1728, 2012.

[23] P. Blomgren and T.F. Chan, "Color TV: total variation methods for restoration of vector-valued images," *IEEE Trans. Image Process.*, vol. 7, no. 3, pp. 304–309, Mar. 1998.

[24] H. Attouch, G. Buttazzo, and G. Michaille, *Variational Analysis in Sobolev and BV Spaces: Applications to PDEs and Optimization*, MPS-SIAM Series on Optimization, 2006.

[25] C. Zach, T. Pock, and H. Bischof, "A duality based approach for realtime TV-L1 optical flow," in *Proceedings of DAGM Symposium on Pattern Recognition*, Berlin, Heidelberg, Sep. 12-14, 2007, pp. 214–223, Springer-Verlag.

[26] V. Duval, J.-F. Aujol, and L. Vese, "Projected gradient based color image decomposition," in *Scale Space and Variational Methods in Computer Vision*, vol. 5567 of *Lecture Notes in Computer Science*, pp. 295–306. Springer Berlin / Heidelberg, 2009.

[27] S. Di Zenzo, "A note on the gradient of a multi-image," *Computer Vision, Graphics and Image Processing*, vol. 33, no. 1, pp. 116–125, Jan. 1986.

[28] G. Sapiro and D. L. Ringach, "Anisotropic diffusion of multivalued images with applications to color filtering," *IEEE Trans. Image Process.*, vol. 5, no. 11, pp. 1582–1586, Nov. 1996.

[29] N. Sochen, R. Kimmel, and R. Malladi, "A general framework for low level vision," *IEEE Trans. Image Process.*, vol. 7, no. 3, pp. 310–318, Mar. 1998.

[30] J. Weickert, "Coherence-enhancing diffusion of colour images," *Image and Vision Computing*, vol. 17, no. 3-4, pp. 201 – 212, Mar. 1999.

[31] D. Tschumperlé and R. Deriche, "Constrained and unconstrained PDE's for vector image restoration," in *Scandinavian Conference on Image Analysis*, Bergen, Norway, Jun. 11-14, 2001.

[32] X. Bresson and T. F. Chan, "Fast dual minimization of the vectorial total variation norm and applications to color image processing," *Inverse Prob. Imaging*, vol. 2, no. 4, pp. 455–484, Nov. 2008.

[33] M. Jung, X. Bresson, T. F. Chan, and L. A. Vese, "Nonlocal Mumford-Shah regularizers for color image restoration," *IEEE Trans. Image Process.*, vol. 20, no. 6, pp. 1583–1598, June 2011.

[34] B. Goldluecke, E. Strekalovskiy, and D. Cremers, "The natural vectorial total variation which arises from geometric measure theory," *SIAM J. Imaging Sci.*, vol. 5, no. 2, pp. 537–563, 2012.

[35] D. C. Youla and H. Webb, "Image restoration by the method of convex projections. Part I - Theory," *IEEE Trans. Med. Imag.*, vol. 1, no. 2, pp. 81–94, Oct. 1982.

[36] H. J. Trussell and M. R. Civanlar, "The feasible solution in signal restoration," *IEEE Trans. Acous. Speech Signal Process.*, vol. 32, no. 2, pp. 201–212, Apr. 1984.

[37] P. L. Combettes, "Inconsistent signal feasibility problems: least-squares solutions in a product space," *IEEE Trans. Signal Process.*, vol. 42, no. 11, pp. 2955–2966, Nov. 1994.

[38] K. Kose, V. Cevher, and A. E. Cetin, "Filtered variation method for denoising and sparse signal processing," in *Proc. Int. Conf. Acoust., Speech Signal Process.*, Kyoto, Japan, Mar. 25-30, 2012, pp. 3329–3332.

[39] T. Teuber, G. Steidl, and R. H. Chan, "Minimization and parameter estimation for seminorm regularization models with I-divergence constraints," *Inverse Problems*, vol. 29, pp. x+29, 2013.

[40] C. Studer, W. Goldstein, T. Yin, and R. G. Baraniuk, "Democratic representations," Jan. 2014, Preprint: http://arxiv.org/pdf/1401.3420v1.pdf.

[41] J.-B. Hiriart-Urruty and C. Lemaréchal, *Convex analysis and minimization algorithms, Part I : Fundamentals*, vol. 305 of *Grundlehren der mathematischen Wissenschaften*, Springer-Verlag, Berlin, Heidelberg, N.Y., 2nd edition, 1996.

[42] E. Van Den Berg and M. P. Friedlander, "Probing the Pareto frontier for basis pursuit solutions," *SIAM J. Sci. Comput.*, vol. 31, no. 2, pp. 890–912, Nov. 2008.

[43] A. Quattoni, X. Carreras, M. Collins, and T. Darrell, "An efficient projection for $\ell_{1,\infty}$ regularization," in *International Conference on Machine Learning*, Montreal, Quebec, Jun. 14-18, 2009, pp. 857–864.

[44] K. Bernard, Y. Tarabalka, J. Angulo, J. Chanussot, and J. A. Benediktsson, "Spectralspatial classification of hyperspectral data based on a stochastic minimum spanning forest approach," *IEEE Trans. Image Process.*, vol. 21, no. 4, pp. 2008 – 2021, Apr. 2012.

[45] D. Tschumperlé and R. Deriche, "Vector-valued image regularization with pdes: A common framework for different applications," *IEEE Trans. Pattern Anal. Match. Int.*, vol. 27, no. 4, pp. 506 – 517, Apr. 2005.

[46] Q. Yuan, L. Zhang, and H. Shen, "Hyperspectral image denoising employing a spectral-spatial adaptive total variation model," *IEEE Trans. on Geoscience and Remote Sensing*, vol. 50, no. 10, pp. 3660 – 3677, Oct. 2012.

[47] Q. Cheng, H. Shen, L. Zhang, and P. Li, "Inpainting for remotely sensed images with a multichannel nonlocal total variation model," *IEEE Trans. on Geoscience and Remote Sensing*, vol. 52, no. 1, pp. 175–187, Jan. 2014.

[48] J. Martin-Herrero, "Anisotropic diffusion in the hypercube," *IEEE Trans. on Geoscience and Remote Sensing*, vol. 45, no. 5, pp. 1386 – 1398, May 2007.

[49] R. Mendez-Rial, M. Calvino-Cancela, and J. Martin-Herrero, "Accurate implementation of anisotropic diffusion in the hypercube," *IEEE Geosci. Remote Sens. Lett.*, vol. 7, no. 4, pp. 870–874, 2010.

[50] T. Lin and S. Bourennane, "Survey of hyperspectral image denoising methods based on tensor decompositions," *EURASIP J. Advances Sig. Proc.*, vol. 186, 2013.

[51] E. J. Candès, X Li, Y. Ma, and J. Wright, "Robust principal component analysis?," *Journal of the ACM*, vol. 58, no. 3, pp. 11:1–11:37, May 2011.

[52] D. Hsu, S. M. Kakade, and T. Zhang, "Robust matrix decomposition with sparse corruptions," *IEEE Trans. Inform. Theory*, vol. 57, no. 11, pp. 7221–7234, Nov. 2011.

[53] G. Ely, S. Aeron, and E. L. Miller, "Exploiting structural complexity for robust and rapid hyperspectral imaging," in *Proc. Int. Conf. Acoust., Speech Signal Process.*, Vancouver, Canada, June 2013.

[54] N. Dobigeon, S. Moussaoui, M. Coulon, J.-Y. Tourneret, and A. O. Hero, "Joint bayesian endmember extraction and linear unmixing for hyperspectral imagery," *IEEE Trans. Signal Process.*, vol. 57, no. 11, pp. 4355–4368, 2009.

[55] E. Chouzenoux, M. Legendre, S. Moussaoui, and J. Idier, "Fast constrained least squares spectral unmixing using primal-dual interior point optimization," *IEEE Journal of Selected Topics in Applied Earth Observations and Remote Sensing*, pp. 59–69, 2013.

[56] W.-K Ma, J. Bioucas-Dias, T.-H. Chan, N. Gillis, P. Gader, A. Plaza, Ambikapathi A., and C.-Y. Chi, "A signal processing perspective on hyperspectral unmixing," *IEEE Trans. Signal Process.*, 2014, to appear.

[57] G. W. Stewart, "On the early history of the singular value decomposition," *SIAM Review*, vol. 35, no. 4, pp. 551–566, 1993.

[58] J.-F. Aujol, "Some first-order algorithms for total variation based image restoration," *J. Math. Imag. Vis.*, vol. 34, no. 3, pp. 307–327, July 2009.

[59] A. Foi and G. Boracchi, "Foveated self-similarity in nonlocal image filtering," in *Proc. SPIE Electronic Imaging 2012, Human Vision and Electronic Imaging XVII*, Burlingame (CA), USA, Jan. 2012, vol. 8291.

[60] G. Gilboa and S. Osher, "Nonlocal linear image regularization and supervised segmentation," *Multiscale Model. and Simul.*, vol. 6, no. 2, pp. 595–630, 2007.

[61] G. Chierchia, N. Pustelnik, J.-C. Pesquet, and B. Pesquet-Popescu, "Epigraphical splitting for solving constrained convex formulations of inverse problems with proximal tools," 2012, Preprint: http://arxiv.org/pdf/1210.5844.

[62] S. Harizanov, J.-C. Pesquet, and G. Steidl, "Epigraphical projection for solving least squares Anscombe transformed constrained optimization problems," in *Scale-Space and Variational Methods in Computer Vision*, 2013, vol. 7893, pp. 125–136.

[63] S. Ono and I. Yamada, "Second-order total generalized variation constraint," 2014, preprint.

[64] M Tofighi, K. Kose, and A. E. Cetin, "Signal reconstruction framework based on Projections onto Epigraph Set of a Convex cost function (PESC)," 2014, preprint.

[65] R. T. Rockafellar and R. J.-B. Wets, *Variational analysis*, Springer-Verlag, 2004.

[66] I. Daubechies, M. Defrise, and C. De Mol, "An iterative thresholding algorithm for linear inverse problems with a sparsity constraint," *Comm. Pure Applied Math.*, vol. 57, no. 11, pp. 1413–1457, Nov. 2004.

[67] C. Chaux, P. L. Combettes, J.-C. Pesquet, and V. R. Wajs, "A variational formulation for frame-based inverse problems," *Inverse Problems*, vol. 23, no. 4, pp. 1495–1518, Jun. 2007.

[68] P. L. Combettes and J.-C. Pesquet, "A Douglas-Rachford splitting approach to nonsmooth convex variational signal recovery," *IEEE J. Selected Topics Signal Process.*, vol. 1, no. 4, pp. 564–574, Dec. 2007.

[69] M. Figueiredo, R. Nowak, and S. Wright, "Gradient projection for sparse reconstruction: application to compressed sensing and other inverse problems," *IEEE J. Selected Topics Signal Process.: Special Issue on Convex Optimization Methods for Signal Processing*, vol. 5981, no. 4, pp. 586–598, Dec. 2007.

[70] A. Beck and M. Teboulle, "A fast iterative shrinkage-thresholding algorithm for linear inverse problems," *SIAM J. Imaging Sci.*, vol. 2, no. 1, pp. 183–202, 2009.

[71] M. Fornasier and C.-B. Schönlieb, "Subspace correction methods for total variation and ℓ_1-minimization," *IMA J. Numer. Anal.*, vol. 47, no. 8, pp. 3397–3428, 2009.

[72] G. Steidl and T. Teuber, "Removing multiplicative noise by Douglas-Rachford splitting methods," *J. Math. Imag. Vis.*, vol. 36, no. 3, pp. 168–184, 2010.

[73] P. L. Combettes and J.-C. Pesquet, "Proximal splitting methods in signal processing," in *Fixed-Point Algorithms for Inverse Problems in Science and Engineering*, H. H. Bauschke, R. S. Burachik, P. L. Combettes, V. Elser, D. R. Luke, and H. Wolkowicz, Eds., pp. 185–212. Springer-Verlag, New York, 2011.

[74] J.-C. Pesquet and N. Pustelnik, "A parallel inertial proximal optimization method," *Pac. J. Optim.*, vol. 8, no. 2, pp. 273–305, Apr. 2012.

[75] G. Chen and M. Teboulle, "A proximal-based decomposition method for convex minimization problems," *Math. Program.*, vol. 64, pp. 81–101, 1994.

[76] E. Esser, X. Zhang, and T. Chan, "A general framework for a class of first order primal-dual algorithms for convex optimization in imaging science," *SIAM J. Imaging Sci.*, vol. 3, no. 4, pp. 1015–1046, 2010.

[77] A. Chambolle and T. Pock, "A first-order primal-dual algorithm for convex problems with applications to imaging," *J. Math. Imag. Vis.*, vol. 40, no. 1, pp. 120–145, 2011.

[78] L. M. Briceño-Arias and P. L. Combettes, "A monotone + skew splitting model for composite monotone inclusions in duality," *SIAM J. Opt.*, vol. 21, no. 4, pp. 1230–1250, 2011.

[79] P. L. Combettes and J.-C. Pesquet, "Primal-dual splitting algorithm for solving inclusions with mixtures of composite, Lipschitzian, and parallel-sum type monotone operators," *Set-Valued Var. Anal.*, vol. 20, no. 2, pp. 307–330, Jun. 2012.

[80] B. C. Vũ, "A splitting algorithm for dual monotone inclusions involving cocoercive operators," *Adv. Comput. Math.*, vol. 38, no. 3, pp. 667–681, Apr. 2013.

[81] L. Condat, "A primal-dual splitting method for convex optimization involving Lipschitzian, proximable and linear composite terms," *J. Optim. Theory Appl.*, vol. 158, no. 2, pp. 460–479, Aug. 2012.

[82] P. Chen, J. Huang, and X. Zhang, "A primal-dual fixed point algorithm for convex separable minimization with applications to image restoration," *Inverse Problems*, vol. 29, no. 2, 2013.

[83] J. J. Moreau, "Proximité et dualité dans un espace hilbertien," *Bull. Soc. Math. France*, vol. 93, pp. 273–299, 1965.

[84] J. Eckstein and D. P. Bertsekas, "On the Douglas-Rachford splitting method and the proximal point algorithm for maximal monotone operators," *Mathematical Programming*, vol. 55, pp. 293–318, 1992.

[85] S. Setzer, G. Steidl, and T. Teuber, "Deblurring Poissonian images by split Bregman techniques," *J. Visual Communication and Image Representation*, vol. 21, no. 3, pp. 193–199, Apr. 2010.

[86] M. V. Afonso, J. M. Bioucas-Dias, and M. A. T. Figueiredo, "An augmented Lagrangian approach to the constrained optimization formulation of imaging inverse problems," *IEEE Trans. Image Process.*, vol. 20, no. 3, pp. 681–695, Mar. 2011.

[87] J. Eckstein, "Parallel alternating direction multiplier decomposition of convex programs," *J. Optim. Theory Appl.*, vol. 80, no. 1, pp. 39–62, 1994.

[88] P. L. Combettes and J.-C. Pesquet, "A proximal decomposition method for solving convex variational inverse problems," *Inverse Problems*, vol. 24, no. 6, Dec. 2008.

[89] M. V. Afonso, J. M. Bioucas-Dias, and M. A. T. Figueiredo, "Fast image recovery using variable splitting and constrained optimization," *IEEE Trans. Image Process.*, vol. 19, no. 9, pp. 2345–2356, 2010.

[90] N. Pustelnik, J.-C. Pesquet, and C. Chaux, "Relaxing tight frame condition in parallel proximal methods for signal restoration," *IEEE Trans. Signal Process.*, vol. 60, no. 2, pp. 968–973, Feb. 2012.

[91] G. Peyré and J. Fadili, "Group sparsity with overlapping partition functions," in *Proc. Eur. Sig. and Image Proc. Conference*, Barcelona, Spain, Aug. 29 – Sept. 2, 2011.

[92] P. Weiss, L. Blanc-Féraud, and G. Aubert, "Efficient schemes for total variation minimization under constraints in image processing," *SIAM J. Sci. Comput.*, vol. 31, no. 3, pp. 2047–2080, Apr. 2009.

[93] J. M. Fadili and G. Peyré, "Total variation projection with first order schemes," *Trans. Img. Proc.*, vol. 20, no. 3, pp. 657–669, Mar. 2011.